The Astrophysical Journal Letters, 982:L31 (10pp), 2025 March 20 https://doi.org/10.3847/2041-8213/adbbef

Self-consistent Multidimensional Penrose Process Driven by Magnetic Reconnection

Filippo Camilloni[1] and Luciano Rezzolla[1,2,3]
[1] Institut für Theoretische Physik, Goethe Universität, Max-von-Laue-Straße 1, 60438 Frankfurt am Main, Germany
[2] School of Mathematics, Trinity College, Dublin 2, Ireland
[3] Frankfurt Institute for Advanced Studies, Ruth-Moufang-Str. 1, 60438 Frankfurt am Main, Germany
Received 2025 January 5; revised 2025 February 27; accepted 2025 February 28; published 2025 March 20

Abstract

Astronomical observations and numerical simulations are providing increasing evidence that resistive effects in plasmas around black holes (BHs) play an important role in determining the phenomenology observed from these objects. In this spirit, we present a general approach to the study of a Penrose process driven by plasmoids that are produced at reconnection sites along current sheets. Our formalism is meant to determine the physical conditions that make a plasmoid-driven Penrose process energetically viable, and can be applied to scenarios that are dominated by matter or magnetic field, that is, in magnetohydrodynamical or force-free descriptions. By exploring reconnection from an axisymmetric but curved surface, our approach can be considered genuinely multidimensional and allows us to explore conditions that are beyond the ones explored so far and that have been restricted to the equatorial plane. Furthermore, it provides a direct contact with numerical simulations of accretion onto BHs, which exhibit an intense reconnection activity outside the equatorial plane. Finally, to describe the kinematics of the plasma self-consistently, we use the well-known configuration of an equilibrium torus with a purely toroidal magnetic field. For such a torus, we discuss the existence of an "ergobelt," i.e., a nontrivial surface penetrating the ergosphere and acting as a natural site for the occurrence of reconnection, and from where we estimate the energetics of a plasmoid-driven Penrose process.

Unified Astronomy Thesaurus concepts: Black hole physics (159); Penrose process (1204); Ergosphere (472); High energy astrophysics (739); Black holes (162); Classical black holes (249); Rotating black holes (1406); Astrophysical black holes (98); Kerr black holes (886); Magnetohydrodynamics (1964); Plasma astrophysics (1261); Magnetic fields (994)

1. Introduction

In a resistive plasma, magnetic reconnection consists in a sudden rearrangement of the magnetic field topology caused by the local interaction of field lines with opposite polarity. This process leads to a rapid conversion of magnetic energy into thermal and kinetic energy of two plasma outflows with locally isotropic properties and moving in opposite directions at relativistic speeds, the plasmoids. The ubiquitous and fundamental role played by magnetic reconnection in astrophysical plasmas is now widely recognized on scales ranging from stellar flares and coronal mass ejections (E. G. Zweibel & M. Yamada 2009; M. Yamada et al. 2010; Y. Su et al. 2013), to high-energy sources such as pulsar magnetospheres (D. A. Uzdensky & A. Spitkovsky 2013), accreting black holes (BHs; A. M. Beloborodov 2017; K. Akiyama et al. 2019; B. Ripperda et al. 2019; Event Horizon Telescope Collaboration et al. 2022), and binary neutron star mergers leading to the short gamma-ray burst phenomenology (M. Anderson et al. 2008; Y. T. Liu et al. 2008; C. Palenzuela et al. 2009; L. Rezzolla et al. 2011; C. Palenzuela et al. 2013; K. Dionysopoulou et al. 2015; K. Kiuchi et al. 2015).

Recent analytic studies, as well as numerical simulations, either in magnetohydrodynamics (MHD) or with particle-in-cell (PIC) approaches, have unfolded a rich phenomenology associated with magnetic reconnection and plasmoid generation, thus enhancing our understanding of these processes both in special-relativistic regimes (L. Comisso & F. A. Asenjo 2014; F. Guo et al. 2014; F. A. Asenjo & L. Comisso 2015; Y.-H. Liu et al. 2015; Y.-H. Liu et al. 2017; D. Ball et al. 2018; C. Meringolo et al. 2023) and when general-relativistic effects become relevant (S. Koide & K. Arai 2008; F. A. Asenjo & L. Comisso 2017; K. Parfrey et al. 2019; A. Bransgrove et al. 2021; L. Comisso & F. A. Asenjo 2021; Z.-Y. Fan et al. 2024; Y. Shen & H.-Y. YuChih 2025). In this regard, astrophysical BHs constitute unique theoretical laboratories to explore extreme conditions of plasma electrodynamics. Indeed, one the most remarkable predictions of general relativity is the possibility of extracting the rotational energy of a BH by invoking the negative inflow of energy and angular momentum at the event horizon (J. P. Lasota et al. 2014), with various processes differing only in the physical agent operating the extraction. Notable examples range from single particles associated with the mechanical (R. Penrose & R. M. Floyd 1971; R. Ruffini et al. 2025) and the collisional Penrose processes process (PP; M. Bañados et al. 2009; M. Bejger et al. 2012; J. D. Schnittman 2014; E. Berti et al. 2015), to superradiant scalar fields (W. H. Press & S. A. Teukolsky 1972; P. Pani et al. 2012; P. Bosch et al. 2016; W. E. East & F. Pretorius 2017), and to force-free electrodynamics (FFE) fields in the Blandford–Znajek (BZ) mechanism (R. D. Blandford & R. L. Znajek 1977; N. Dadhich et al. 2018).

Given the presence of strong magnetic fields and relativistic plasmas near astrophysical BHs, it is natural to expect a manifestation of the PP triggered by magnetic reconnection and mediated by plasmoids. This idea was originally proposed and explored analytically by S. Koide & K. Arai (2008), to be further reviewed and extended by F. A. Asenjo & L. Comisso (2017)

and L. Comisso & F. A. Asenjo (2021), who computed the power extracted and the efficiency of the process in terms of the local reconnection rate (see also K. Parfrey et al. 2019, for related PIC simulations). The basic picture of this process involves a current sheet with large aspect ratio forming within the BH ergosphere. As is ordinary in reconnection processes, such a current sheet fragments via the tearing instability into a chain of plasmoids (or magnetic flux tubes in three dimensions) that are accelerated away from the reconnection layer, becoming an efficient channel to transport magnetic energy away from the reconnection site. In a steady state, pairs of plasmoids are ejected from the reconnection site, where, for each pair, a plasmoid will move outwards to large distances, while the other one will be ingoing and move toward the event horizon. If the ingoing plasmoid has a negative energy-at-infinity, it will drive a PP. It is important to note that the plasmoid that is relevant for the PP is the ingoing one and that it needs to travel only a lengthscale of $\mathcal{O}(M)$ within the ergosphere to reach the event horizon and extract energy via the PP. The details of what happens to the outgoing plasmoid are not important for the success of the PP, and the outgoing plasmoid could transmit its energy-at-infinity just outside the ergosphere after being converted into electromagnetic bursts or at very large distances (e.g., via synchrotron cooling).[4] The PP would work in either case.

Despite the importance of the initial works by S. Koide & K. Arai (2008) and L. Comisso & F. A. Asenjo (2021), they contain a number of approximations that prevent testing them in numerical environments and assessing their viability in realistic astrophysical scenarios. Arguably, the most serious of these limitations rests with the lack of a self-consistent description of the plasma dynamics, either in the MHD or FFE regimes. In turn, this forces the use of a number of assumptions on the dynamics of the plasma that are either far from known solutions and numerical simulations (see, e.g., J. F. Mahlmann et al. 2020; A. Nathanail et al. 2020, 2021; B. Ripperda et al. 2020, 2022; B. Crinquand et al. 2022; I. Dimitropoulos et al. 2024) or difficult to realize in practice.

To overcome these difficulties, it is important to construct reconnection models that are consistent with well-known plasma solutions or that share dynamical features and conditions which are similar to those encountered in simulations. The goal of this work is therefore that of having an analytic understanding of the energetics of the PP mediated by plasmoids for a nontrivial distribution of matter and electromagnetic fields. We do this by exploiting a self-consistent, fully covariant analytic description of plasma and fields of degenerate electrodynamics that includes ideal MHD and FFE as particular examples. More specifically, we analyze, for the first time, the conditions under which a distribution of magnetized matter penetrating the ergosphere and not restricted to the equatorial plane can produce plasmoids with negative energy-at-infinity. In this way, we can study the extraction of energy and angular momentum from a Kerr BH in a self-consistent scenario that is not too far from the conditions explored in simulations. The ultimate expectation is that the insight that will be gained via these analytical calculations will be of help in understanding the results of simulations of the plasmoid-driven PP once they will have reached a sufficient degree of realism.

[4] Radiative losses are important in a realistic description of plasmoids propagating in the surrounding plasma, and we expect these losses to be particularly relevant for those plasmoids traveling large distances of $\mathcal{O}(100\,M)$ (N. Aimar et al. 2023) and for which synchrotron cooling can be effective. Radiative losses will instead affect only mildly those plasmoids that propagate from within the ergoregion to the event horizon, as they travel much shorter lengths of $\mathcal{O}(M)$.

2. Degenerate Electrodynamics around a Kerr BH

We consider the electrodynamics of a Kerr BH with mass M and specific angular momentum a. Following K. S. Thorne & D. Macdonald (1982), and introducing $\boldsymbol{F}$ and $\eta_{\mu\nu\rho\sigma}$, respectively, as the Faraday tensor and the Levi-Civita symbol, we refer to as *degenerate* those electromagnetic fields that satisfy the condition $\eta_{\mu\nu\rho\sigma}F^{\mu\nu}F^{\rho\sigma}=0$ (or, equivalently, satisfying the condition of orthogonality between the electric and magnetic fields $\boldsymbol{E}\cdot\boldsymbol{B}=0$), and as *magnetically dominated* if $F_{\mu\nu}F^{\mu\nu}>0$ (or, equivalently, if $B^2-E^2>0$). Under this definition, force-free electromagnetic fields are clearly degenerate, but degeneracy can occur more generally and, indeed, an electromagnetic field can be degenerate without being force-free. This is because degeneracy appears whenever the electric field in the rest frame of the plasma vanishes, i.e., when $\boldsymbol{F}\cdot\boldsymbol{u}=0$, where $\boldsymbol{u}$ is the plasma four-velocity. Clearly, a plasma with infinite conductivity, such as that characterizing the ideal-MHD limit, will have a zero comoving electric field and hence will be degenerate but not force-free. As a result, the conditions of a degenerate and magnetically dominated plasma describe both the force-free and the ideal-MHD conditions (see also S. E. Gralla & T. Jacobson 2014; A. Chael et al. 2023; Y. Mizuno & L. Rezzolla 2024, for more recent discussions). The orthogonality of electric and magnetic fields are violated only on the microscopical scales of the current sheets where reconnection takes place (Y.-H. Liu et al. 2017). Degeneracy also implies that stationary and axisymmetric fields are expressed in terms of a magnetic flux function $\Psi=\Psi(r,\,\theta)$ that, under a suitable gauge choice, coincides with the toroidal component of the electromagnetic potential. As a result, constant-Ψ surfaces determine the poloidal magnetic fields, the poloidal current $I=I(r,\,\theta)$, which is proportional to the toroidal field, and the angular velocity of the magnetic field lines $\Omega=\Omega(\Psi)$ (S. E. Gralla & T. Jacobson 2014).[5]

2.1. Zero-angular-momentum Observer Frame

A 3+1 decomposition of spacetime has a long history in BH electrodynamics (K. S. Thorne & D. Macdonald 1982; L. D. Landau & E. M. Lifshitz 2004), since it provides equations in a form that closely resembles the classical Maxwell equations, and can then be employed in numerical simulations. In this case, the metric can be written in terms of the lapse function α, the shift vector β^{ϕ}, and the spatial metric γ_{ij} (see L. Rezzolla & O. Zanotti 2013; also see Appendix A). Within this decomposition, a particularly convenient class of observers with a long history of use in the literature (J. M. Bardeen et al. 1972) is that with zero angular momentum (ZAMO) with a worldline tangent

$$\boldsymbol{\eta} := \eta^{\mu}\boldsymbol{\partial}_{\mu}=\alpha^{-1}(\boldsymbol{\partial}_{t}+\omega_{Z}\boldsymbol{\partial}_{\phi}), \tag{1}$$

[5] Despite retaining axisymmetry as a working assumption, our approach is multidimensional, as the current sheets associated with such configurations are off-equatorial and described by surfaces extending in the polar, azimuthal, and radial directions. This is in contrast with equatorial current sheets, which only span the latter two.

and whose angular velocity is $\omega_Z := -\beta^\phi$. Such an observer carries a local orthonormal (Cartesian) tetrad, $\hat{\boldsymbol{e}}_{(\alpha)}$, with $\alpha = T, X, Y, Z$, such that on the equatorial plane ($\theta = \pi/2$) the X and Y legs align with the r and ϕ directions, respectively, whereas the Z leg is orthogonal to the equatorial plane and parallel to the BH spin (quantities in the ZAMO frame are marked with a "hat" and the components with bracketed indices).

Introducing ${}^*\boldsymbol{F}$ as the dual of the Faraday tensor, the magnetic field measured by the ZAMO, $\hat{\mathcal{B}}^\mu := -{}^*F^{\mu\nu}\eta_\nu$, is purely spacelike, and in ZAMO-adapted coordinates one has that $\hat{\boldsymbol{\mathcal{B}}} = \hat{\mathcal{B}}^{(\alpha)}\hat{\boldsymbol{e}}_{(\alpha)}$ reads

$$\hat{\boldsymbol{\mathcal{B}}} = \frac{\partial_\theta \Psi}{\sqrt{\Pi}\sin\theta}\hat{\boldsymbol{e}}_{(X)} - \frac{I}{\sqrt{\Delta}\sin\theta}\hat{\boldsymbol{e}}_{(Y)} + \frac{\sqrt{\Delta}\,\partial_r \Psi}{\sqrt{\Pi}\sin\theta}\hat{\boldsymbol{e}}_{(Z)}, \tag{2}$$

where

$$\Delta := r^2 - 2Mr + a^2, \tag{3}$$

$$\Pi := (r^2 + a^2)^2 - a^2\Delta\sin^2\theta \tag{4}$$

are two metric functions of the Kerr solution, and with the positions of the outer and inner horizons $r_\pm$ given by roots of $\Delta = (r - r_+)(r - r_-)$ (see also Appendix A).

The electric field, $\hat{\mathcal{E}}^\mu := F^{\mu\nu}\eta_\nu$, is orthogonal to $\hat{\boldsymbol{\mathcal{B}}}$ and in the ZAMO basis $\hat{\boldsymbol{\mathcal{E}}} = \hat{\mathcal{E}}^{(\alpha)}\hat{\boldsymbol{e}}_{(\alpha)}$ reads

$$\hat{\boldsymbol{\mathcal{E}}} = \frac{\sqrt{\gamma_{\phi\phi}}}{\alpha}(\omega_Z - \Omega)(\hat{\mathcal{B}}^{(Z)}\hat{\boldsymbol{e}}_{(X)} - \hat{\mathcal{B}}^{(X)}\hat{\boldsymbol{e}}_{(Z)}), \tag{5}$$

so that it is possible to interpret $\hat{\boldsymbol{v}}_F = \sqrt{\gamma_{\phi\phi}}/\alpha(\Omega - \omega_Z)\hat{\boldsymbol{e}}_{(Y)}$ as the field lines' velocity in the ZAMO frame, and recover the usual expression $\hat{\boldsymbol{\mathcal{E}}} = -\hat{\boldsymbol{v}}_F \times \hat{\boldsymbol{\mathcal{B}}}$.

The orthogonality of the electric and magnetic fields to each other and to the ZAMO four-velocity implies the following set of orthonormal vectors (J. C. McKinney 2006; A. Chael et al. 2023):

$$\mathcal{T}^{(\alpha)} := \eta^{(\alpha)}, \quad \mathcal{X}^{(\alpha)} := \frac{\hat{\mathcal{E}}^{(\alpha)}}{\sqrt{\mathcal{E}^2}}, \quad \mathcal{Y}^{(\alpha)} := \frac{\hat{\mathcal{B}}^{(\alpha)}}{\sqrt{\mathcal{B}^2}},$$
$$\mathcal{Z}^{(\alpha)} := \epsilon^{(\alpha)(\beta)(\gamma)(\delta)}\mathcal{T}_{(\beta)}\mathcal{X}_{(\gamma)}\mathcal{Y}_{(\delta)}. \tag{6}$$

The plasma four-velocity in the ZAMO frame, $\hat{\boldsymbol{u}} = \hat{u}^{(\alpha)}\hat{\boldsymbol{e}}_{(\alpha)}$, admits the generic decomposition in terms of components which are parallel, $\parallel$, or orthogonal, $\perp$, with respect to the magnetic field lines (S. S. Komissarov 2004; J. C. McKinney 2006; A. Chael et al. 2023; Z. Gelles et al. 2025):

$$\hat{\boldsymbol{u}} = \hat{\gamma}(\boldsymbol{\mathcal{T}} + \hat{v}_\parallel \boldsymbol{\mathcal{Y}} + \hat{v}_\perp \boldsymbol{\mathcal{Z}})\,. \tag{7}$$

Such a decomposition has the advantage that the spatial velocity orthogonal to the fields is solely specified by the electromagnetic sector, $\hat{v}_\perp := \mathcal{E}/\mathcal{B}$, and the corresponding Lorentz factor is $\hat{\gamma}_\perp := \sqrt{\mathcal{B}^2/(\mathcal{B}^2 - \mathcal{E}^2)}$, where $\mathcal{B}^2 - \mathcal{E}^2 > 0$. The total Lorentz factor, $\hat{\gamma}$, is given by

$$\hat{\gamma} := \frac{1}{\sqrt{1 - \hat{v}_\perp^2 - \hat{v}_\parallel^2}}, \tag{8}$$

and we note that flows with $\hat{\gamma} = \hat{\gamma}_\perp$ (i.e., with $\hat{v}_\parallel = 0$) provide a uniquely covariant definition of timelike observers in FFE characterized by $\boldsymbol{E} \times \boldsymbol{B}$ drift velocities (J. C. McKinney 2006). Since the total Lorentz factor can also be expressed as $\hat{\gamma}^2 = \hat{\gamma}_\perp^2/(1 - \hat{\gamma}_\perp^2\hat{v}_\parallel^2)$, it follows that $\hat{\gamma} \geqslant \hat{\gamma}_\perp$, namely, $\hat{\gamma} = \hat{\gamma}_\perp$ for $\hat{v}_\parallel = 0 =: \hat{v}_\parallel^{\min}$, and $\hat{\gamma} \to \infty$ for $\hat{v}_\parallel = \hat{\gamma}_\perp^{-1} =: \hat{v}_\parallel^{\max}$ (A. Chael et al. 2023).

2.2. Comoving Frame

Because reconnection is normally studied locally, i.e., in the frame comoving with the plasma (Y.-H. Liu et al. 2017), we introduce the comoving frame with a timelike tangent given by the plasma four-velocity $\hat{\boldsymbol{u}}$. In the ideal-MHD limit of infinite electrical conductivity, any electric field is zero in the frame comoving with the fluid, so that if we define the electric, $\boldsymbol{e}$, and magnetic, $\boldsymbol{b}$, fields in the comoving frame, respectively, as $e^\mu := F^{\mu\nu}u_\nu$ and $b^\mu := -{}^*F^{\mu\nu}u_\nu$, then $e^\mu = 0$ by construction. Note that while we will employ a comoving frame to compute the details of the reconnection and plasmoid production, we will always make use of the electromagnetic fields in the ZAMO frame, $\hat{\boldsymbol{\mathcal{E}}}$ and $\hat{\boldsymbol{\mathcal{B}}}$, so that the comoving magnetic field is

$$\boldsymbol{b} := \frac{\hat{\boldsymbol{\mathcal{B}}} + (\hat{\boldsymbol{u}} \cdot \hat{\boldsymbol{\mathcal{B}}})\hat{\boldsymbol{u}}}{\hat{\gamma}}, \tag{9}$$

and $b^2 := \boldsymbol{b} \cdot \boldsymbol{b} = \mathcal{B}^2 - \mathcal{E}^2$.

In the frame comoving with the fluid, we assume that two plasmoids are ejected locally tangent to the current sheet with opposite "outflow" velocities $\pm\,\tilde{v}_{\rm out}$, where the signs distinguish the plasmoid ejected in the direction parallel (+) or antiparallel (−) to the comoving magnetic field lines as seen from one side of the reconnection layer.[6] The initial outflow four-velocity of the plasmoids is thus

$$\tilde{\boldsymbol{u}}_{\rm out} = \tilde{\gamma}_{\rm out}(\hat{\boldsymbol{u}} \pm \tilde{v}_{\rm out}\ \ \boldsymbol{b}/b), \tag{10}$$

with the azimuthal velocity and Lorentz factor in the ZAMO basis given by

$$\hat{v}_{\rm out}^{(Y)} = \frac{(\hat{\gamma}_\perp\hat{v}_\parallel \pm \tilde{v}_{\rm out})\hat{\mathcal{B}}^{(Y)}}{\hat{\gamma}_\perp(1 \pm \hat{\gamma}_\perp\hat{v}_\parallel\tilde{v}_{\rm out})\mathcal{B}} - \hat{v}_\perp\frac{\sqrt{\hat{\mathcal{B}}_{(X)}^2 + \hat{\mathcal{B}}_{(Z)}^2}}{\mathcal{B}}, \tag{11}$$

$$\hat{\gamma}_{\rm out} = \hat{\gamma}\tilde{\gamma}_{\rm out}(1 \pm \hat{\gamma}_\perp\hat{v}_\parallel\tilde{v}_{\rm out})\,. \tag{12}$$

2.3. Plasmoids, Relativistic Adiabatic Incompressible Balls, and the Penrose Process

To define the details of the PP, we need a local model for magnetic reconnection that provides a prescription for the velocity field $\tilde{v}_{\rm out}$ of the plasmoids and their energetics. Such a model will have to account for the redistribution of the magnetic energy into the kinetic and internal energy of the plasmoid. The details of this conversion, which we here assume to originate from a hydrogen plasma, can be extremely difficult to calculate under realistic conditions, and probably require a microscopical description involving PIC simulations (D. Ball et al. 2018; C. Meringolo et al. 2023). However, the most important reconnection quantities that we consider here, namely, the outflow velocity and the reconnection rate, emerge from MHD constraints and, as argued by Y.-H. Liu et al. (2017), are not sensitive to the microphysics in so long as reconnection is mediated by plasmoids and the upstream plasma is in the collisionless regime (L. Comisso & F. A. Asenjo 2021).

[6] Under realistic conditions such as those exhibited by the numerical simulations, plasmoids of different sizes and velocities are expected to be produced, so that $\tilde{v}_{\rm out}$ will actually follow a distribution (Y.-M. Huang & A. Bhattacharjee 2012).

Approximate expressions for these quantities are given by

$$\tilde{v}_{\rm out} \approx \sqrt{\sigma_0/(1+\sigma_0)}, \qquad \mathcal{R}_{\rm rec} \simeq 0.1, \tag{13}$$

with σ_0 being the upstream plasma magnetization.

Moreover, to make some analytic progress, we use a so-called relativistic adiabatic incompressible ball (RAIB) model (S. Koide & K. Arai 2008), normally adopted under these conditions (see F. A. Asenjo & L. Comisso 2017; L. Comisso & F. A. Asenjo 2021, and related works). Notwithstanding some of their limitations, RAIBs represent the simplest yet nontrivial model of plasmoids, which are treated as localized distributions of energy dressed with an additional pressure term that contributes to their inertia and is reminiscent of their hydrodynamical nature. The RAIB energy-at-infinity needed to estimate the extraction of energy from a reconnection-driven PP follows upon integrating the energy-momentum tensor of a perfect fluid, and reads (see S. Koide & K. Arai 2008; see also Appendix D)

$$E^{\infty} = \alpha H\left[\hat{\gamma}_{\rm out}\left(1+\frac{\sqrt{\gamma_{\phi\phi}}}{\alpha}\omega_{\rm Z}\hat{v}^{(Y)}_{\rm out}\right) - \frac{U(\Gamma-1)}{H\quad\hat{\gamma}_{\rm out}}\right], \tag{14}$$

with H, U, and Γ the total enthalpy, internal energy, and adiabatic index in the plasmoid, respectively.

Hence, the energy-at-infinity per unit enthalpy, $\varepsilon^{\infty} := E^{\infty}/H$, is

$$\begin{aligned}\varepsilon^{\infty}_{\pm} = \alpha\hat{\gamma}\Bigg[&\left(1+\left(\hat{v}_{\parallel}\frac{\hat{\mathcal{B}}^{(Y)}}{\mathcal{B}} - \hat{v}_{\perp}\frac{\sqrt{\hat{\mathcal{B}}^2_{(X)}+\hat{\mathcal{B}}^2_{(Z)}}}{\mathcal{B}}\right)\frac{\sqrt{\gamma_{\phi\phi}}}{\alpha}\omega_{\rm Z}\right)\tilde{\gamma}_{\rm out}+\\ &\pm\left(\hat{v}_{\parallel}\hat{\gamma}_{\perp}+\left(\frac{\hat{\mathcal{B}}^{(Y)}}{\hat{\gamma}_{\perp}\mathcal{B}} - \hat{v}_{\parallel}\hat{v}_{\perp}\hat{\gamma}_{\perp}\frac{\sqrt{\hat{\mathcal{B}}^2_{(X)}+\hat{\mathcal{B}}^2_{(Z)}}}{\mathcal{B}}\right)\frac{\sqrt{\gamma_{\phi\phi}}}{\alpha}\omega_{\rm Z}\right)\\ &\times\tilde{v}_{\rm out}\tilde{\gamma}_{\rm out} - \frac{U(\Gamma-1)/H}{\hat{\gamma}^2\tilde{\gamma}_{\rm out}(1\pm\hat{\gamma}_{\perp}\hat{v}_{\parallel}\tilde{v}_{\rm out})}\Bigg].\end{aligned} \tag{15}$$

Equation (15) contains information not only on the background geometry via the metric functions α, $\omega_{\rm z}$, and $\gamma_{\phi\phi}$, but also on the global magnetic field configuration around the BH, either via the magnetic field components $\hat{\mathcal{B}}^{(\alpha)}$ or through the field strength given by $\hat{v}_{\perp} = \mathcal{E}/\mathcal{B}$. In addition, the dynamics of the bulk plasma is encoded in $\hat{v}_{\parallel}$, which should be prescribed together with the coordinate invariant quantities $\Psi(r,\theta)$, $I(r,\theta)$, and $\Omega(\Psi)$. Note that Equation (15) is consistent with any stationary and axisymmetric solution in ideal MHD and in FFE, and can be used to model BH energy extraction by plasmoids in more realistic configurations. In contrast, previous models were restricted to the equatorial plane and invoked a Keplerian dynamics that is not realistic within the ergosphere (S. Koide & K. Arai 2008; F. A. Asenjo & L. Comisso 2017; L. Comisso & F. A. Asenjo 2021).

3. Application to a Magnetized Torus

All studies to date of reconnection-driven PP have been restricted to scenarios where current sheets develop on the BH equatorial plane. However, there is growing numerical evidence, either from MHD (J. F. Mahlmann et al. 2020; A. Nathanail et al. 2020, 2021; B. Ripperda et al. 2020, 2022; I. Dimitropoulos et al. 2024) or from PIC simulations (I. El Mellah et al. 2022, 2023; J. Vos et al. 2024), that significant reconnection takes place also in the transition zone between the thick accretion disk and the ensuing jet launched by the BH. More specifically, such simulations have shown that the accretion disk around a BH develops a toroidal component and that the transition region between the torus and the funnel systematically leads to reconnection phenomena.

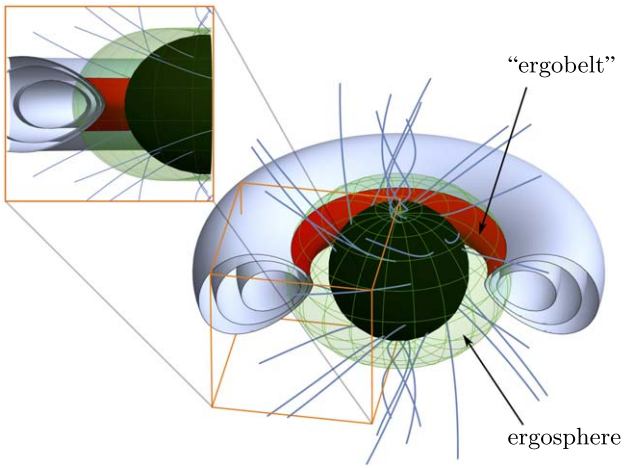

Figure 1. Shown with gray contours are the isolevels of the rest-mass density of a torus with a toroidal magnetic field entering the BH ergosphere (green region). Reconnection and plasmoid production can take place on the surface of the torus; if this happens in the ergoregion, i.e., on the "ergobelt" (red region), then a PP can be activated from plasmoids with a negative energy-at-infinity.

To achieve a treatment in which the off-equatorial dynamics of matter is not prescribed "by hand" (as done so far with equatorial current sheets) but follows self-consistently from a stable fluid configuration, we apply our general treatment to the well-known Komissarov's solution, namely, to a geometrically thick disk endowed with purely toroidal magnetic fields corotating with the BH (S. S. Komissarov 2006; P. J. Montero et al. 2007; S. Gimeno-Soler & J. A. Font 2017). The presence of an inner light surface will naturally lead to dominant toroidal magnetospheric fields in the ergoregion with polarity in the counterrotating direction (S. S. Komissarov 2004; D. A. Uzdensky 2005; S. E. Gralla & T. Jacobson 2014; A. Nathanail & I. Contopoulos 2014; F. Camilloni et al. 2022). Indeed, a necessary condition for the BZ mechanism to occur is $\omega_{\rm BH} > \Omega > 0$ (J. P. Lasota et al. 2014). This implies that the field lines' tension oppose the BH rotation, so that the azimuthal components of the magnetic field must have polarity in the counterrotating direction, $\hat{\mathcal{B}}^{(Y)} = \sqrt{\gamma_{\phi\phi}}\hat{\mathcal{B}}^{\phi} \propto -I \propto -(\omega_{\rm BH}-\Omega) < 0$, close to the event horizon (see, e.g., F. Camilloni et al. 2022, for a derivation).

Hence, with the simultaneous presence of toroidal magnetic fields with corotating polarity within the torus and toroidal magnetospheric fields with counterrotating polarity within the funnel, the accretion-disk surface will develop a current sheet and act as an optimal site for the production of plasmoids, as also found in numerical simulations (I. Dimitropoulos et al. 2024).[7] Furthermore, the portion of the torus surface that is inside the ergosphere and undergoes reconnection, what we dub the "ergobelt" (red region in Figure 1), can generate plasmoids that have negative energy-at-infinity and hence tap the BH rotational energy via a plasmoid-driven PP. Note that

[7] Under realistic conditions of accretion and outside the ergosphere, the magnetic field will also have a poloidal component both in the torus and in the jet, so that the presence of guide fields can be relevant for reconnection taking place far from the ergosphere.

the current sheet on the torus surface will also be accompanied by the standard equatorial current sheet that inevitably develops for split-field configurations; we refer to S. Koide & K. Arai (2008), F. A. Asenjo & L. Comisso (2017), L. Comisso & F. A. Asenjo (2021), K. Parfrey et al. (2019), and B. Chen et al. (2024) for a review of the phenomenology and energetics associated with these current sheets.

Such a magnetized torus thus provides a simplified yet nontrivial configuration that is mathematically self-consistent and does not invoke unrealistic assumptions. The Komissarov solution naturally entails that $\Psi = 0$ and

$$\hat{v}_{\parallel} = \ell_0 \frac{\alpha}{\sqrt{\gamma_{\phi\phi}}(\omega_{\rm Z}\ell_0 - 1)}, \tag{16}$$

so that $\hat{v}_{\perp} = 0$ and $\hat{\mathcal{B}}^{(X)} = \hat{\mathcal{B}}^{(Z)} = 0$ (see Appendix C). Hereafter, we will consider maximally filled tori with $\ell_0 \approx \ell_{\rm mb}$ and $\mathcal{W}_{\rm in} = \mathcal{W}_{\rm cusp} = 0$.

Following S. Koide & K. Arai (2008) and L. Comisso & F. A. Asenjo (2021), we assume the plasmoids/RAIBs to consist of relativistically hot plasma described by an ideal-fluid equation of state so that $H = 4U(\Gamma - 1)$. As mentioned above, and since we are interested in the PP associated with an accretion scenario onto a supermassive BH, the reconnection we envisage to take place at the ergobelt is one that involves a hydrogen plasma. Moreover, we use the analytic model of magnetic reconnection by Y.-H. Liu et al. (2017), with a reconnection electric field proportional to the reconnection rate, and predicting plasmoid velocities that are simple functions of the magnetization $\sigma_0 := b^2/w_0$, where w_0 is the enthalpy density. More specifically, we set (Y. E. Lyubarsky 2005)

$$\tilde{v}_{\rm out} \approx \sqrt{\sigma_0/(1+\sigma_0)}, \qquad \tilde{\gamma}_{\rm out} \approx \sqrt{1+\sigma_0}, \tag{17}$$

so that Equation (15) simplifies and becomes dependent on the BH spin a, the plasma magnetization σ_0,[8] the torus angular momentum ℓ_0, and the $(r,\ \theta)$ location of the ergobelt (see Equation (C1) in Appendix C).

A number of important remarks should be made on $\varepsilon^{\infty}_{\pm}$ as obtained above. First, the value at the event horizon, $\varepsilon^{\infty}_{\pm}|_{r_+}$, is finite for all BH spins. Second, since the conditions for a successful PP require $\varepsilon^{\infty}_{+} > 0$ and $\varepsilon^{\infty}_{-} < 0$ (L. Comisso & F. A. Asenjo 2021), a critical magnetization, $\sigma_{0,\rm crit}$, exists that depends on the BH spin and torus properties and below which no PP can take place. For instance, for $a/M = 0.9$ and $\ell_0/M \lesssim 2.63$, $\sigma_{0,\rm crit} \approx 4.65$, which is consistent with the values observed in the transition region in simulations (A. Nathanail et al. 2020, 2021). Third, in regions where $\sigma_0 \gg 1$, Equation (15) further simplifies to

$$\varepsilon^{\infty}_{\pm} = \sqrt{\sigma_0}\left(1 \pm \frac{\sqrt{\gamma_{\phi\phi}}}{\alpha}\omega_{\rm Z}\right)\sqrt{\frac{1 \pm \hat{v}_{\parallel}}{1 \mp \hat{v}_{\parallel}}}, \tag{18}$$

showing that plasmoids with $\varepsilon^{\infty}_{-} < 0$ can be produced for sufficiently high magnetization, provided that a portion of the torus intersects the ergosphere where $\omega_{\rm Z}\sqrt{\gamma_{\phi\phi}} \geqslant \alpha$. For maximally filled tori, the torus cusp is inside the ergosphere if

$$a > a_{\rm crit} := 2(\sqrt{2} - 1)\, M \approx 0.83\, M\ . \tag{19}$$

Finally, and most importantly, because Equation (15) applied to a torus is not restricted to the equatorial plane, it allows us to study, for the first time, the problem of a plasmoid-driven PP in an axisymmetric but nonequatorial context.

Figure 2 shows polar sections of magnetized tori with $\ell_0 \lesssim \ell_{\rm mb}$ entering the ergosphere of BHs with spin. Marked with a color map are the values of the magnetization σ_0 such that $\varepsilon^{\infty}_{+} > 0$ and $\varepsilon^{\infty}_{-} < 0$ (see Equation (15)) and reported are the corresponding critical values for the magnetization increasing from left to right. For magnetizations above a critical value $\sigma_{0,\rm crit}$, the innermost part of the torus possesses an ergobelt as a site for the production of plasmoids with negative energy-at-infinity and hence yield a PP. Moreover, for faster spinning BHs, larger portions of the torus penetrate the ergosphere, increasing the potential production of plasmoids.

3.1. Energetics of the Plasmoid-driven Penrose Process

Because of the nonlinear nature of reconnection and of the plasma dynamics near the torus surface, the energy-extraction process will be intrinsically stochastic, so that the energy-extraction rate $\dot{E}_{\rm rec}$ will depend on the local reconnection rate, routinely assumed to be $\mathcal{R}_{\rm rec} \simeq 0.1$ (Y.-M. Huang & A. Bhattacharjee 2012; F. A. Asenjo & L. Comisso 2017; P. A. Cassak et al. 2017; Y.-H. Liu et al. 2017; L. Comisso & F. A. Asenjo 2021). Taking now $\mathcal{L}$ and $\mathcal{A}$ respectively as the linear size and surface area of the ergobelt (note there are two ergobelts, symmetric with respect to the equatorial plane), we approximate the enthalpy density as $w_0 \approx H/(\mathcal{L}\mathcal{A})$ and express the energy-extraction rate as

$$\dot{E}_{\rm rec} = -2\,\mathcal{R}_{\rm rec}\, w_0 \int_{\mathcal{A}} \varepsilon^{\infty}_{-} d\mathcal{A} = -2\,\mathcal{R}_{\rm rec}\, w_0\, \mathcal{A}\, \langle \varepsilon^{\infty}_{-} \rangle, \tag{20}$$

where

$$\langle \varepsilon^{\infty}_{-} \rangle := \frac{\int_{\mathcal{A}} \varepsilon^{\infty}_{-} d\mathcal{A}}{\int_{\mathcal{A}} d\mathcal{A}}, \tag{21}$$

is the energy-at-infinity averaged over the area of the ergobelt (see Appendix C).

In the top part of Figure 3, we report the behavior of $\dot{E}_{\rm rec}/w_0$ as a function of the plasma magnetization and BH spin. As expected, no energy extraction occurs if the BH is not spinning sufficiently fast (the torus does not enter the ergosphere) or if the magnetization is below the corresponding critical value (red solid line). Conversely, the process is more efficient for rapidly spinning BHs and high magnetizations, since the effective area of the ergobelt then increases. The values of $\dot{E}_{\rm rec}$ are comparable or larger than those estimated by L. Comisso & F. A. Asenjo (2021) for plasmoids generated in the equatorial plane.

Finally, we can compare the extracted energy via plasmoids with the power extracted via the BZ mechanism, which, we recall, is steady and effective for any nonzero value of the BH spin. The BZ power extracted by a split-monopole field in Kerr can be written as an expansion in the BH angular velocity, $\omega_{\rm BH} := \omega_{\rm Z}|_{r_+}$, to ensure a better convergence (A. Tchekhovskoy et al. 2010;

[8] The typical magnetization just inside the torus is $\sim\mathcal{O}(0.01 - 0.1)$ with vanishing magnetic fields at the surface. Numerical simulations show that σ_0 jumps to $\sim\mathcal{O}(10 - 100)$ just outside the torus (J. F. Mahlmann et al. 2020; A. Nathanail et al. 2020, 2021; B. Ripperda et al. 2020, 2022; I. Dimitropoulos et al. 2024). Hence, to model the reconnection in the transition region in the vicinity of the ergobelt, we consider $0.1 \lesssim \sigma_0 \lesssim 10$.

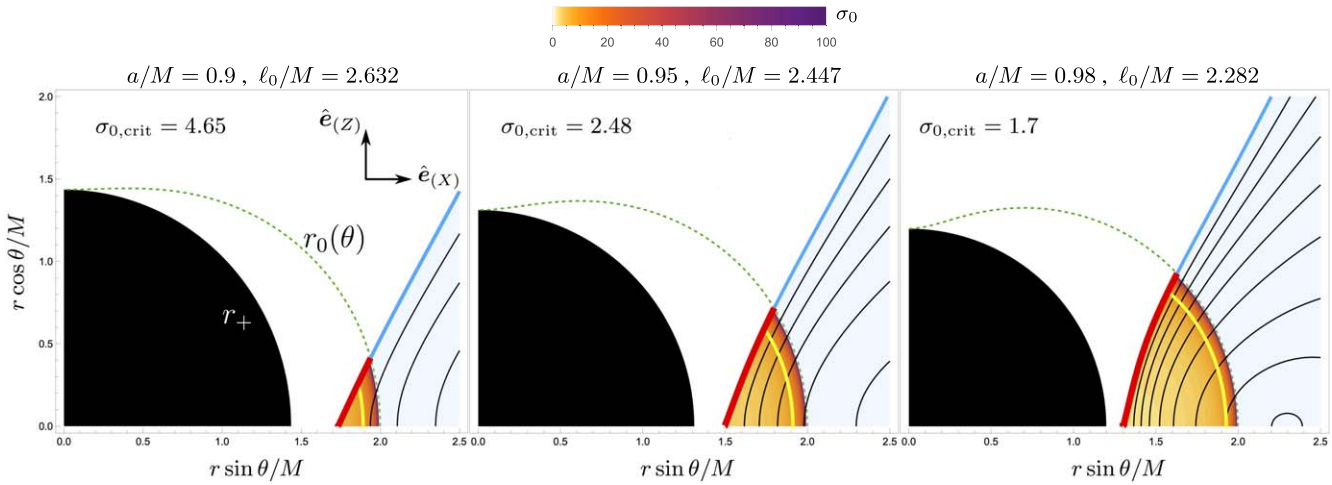

Figure 2. Polar sections of tori with $\ell_0 \simeq \ell_{\rm mb}$ (light blue shading) entering the ergosphere r_0 (green dashed line), with BH spin increasing from left to right. The torus surface inside the ergosphere, dubbed the ergobelt (red solid line), is suitable for reconnection to drive a PP. The color map reports values of the magnetization σ_0 necessary for the pair-production of plasmoids with $\varepsilon_+^\infty > 0$ and $\varepsilon_-^\infty < 0$ at different positions in the torus, with the yellow solid line marking $\sigma_0 = 10$.

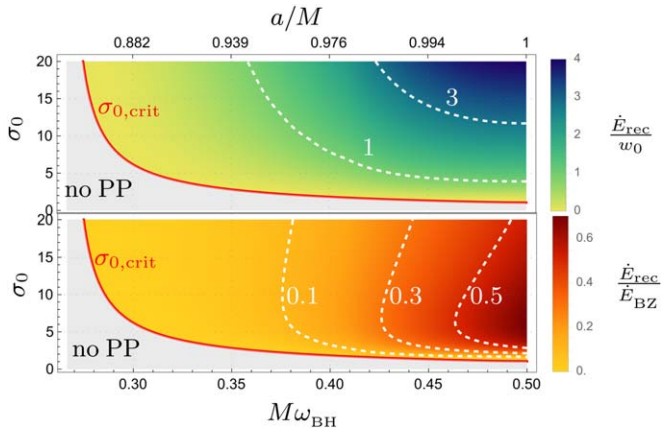

Figure 3. Top panel: rate of energy extraction per unit of enthalpy density, $\dot{E}_{\rm rec}/w_0$, at the ergobelt of a maximally filling torus as a function of the magnetization σ_0 and BH angular velocity $\omega_{\rm BH}$ (the top horizontal axis uses instead a scale in a/M). The red solid line marks the critical magnetization $\sigma_{0,\rm crit}$ below which no PP is possible (gray shaded area). Bottom panel: the same as in the top but when the energy-extraction rate is normalized to the BZ power $\dot{E}_{\rm rec}/\dot{E}_{\rm BZ}$.

F. Camilloni et al. 2022), and reads

$$\dot{E}_{\rm BZ} \simeq \left(\frac{2\pi B_0^2 r_+^2 \omega_{\rm BH}^2}{3}\right) \times [1 + 1.38\,(M\omega_{\rm BH})^2 - 9.2\,(M\omega_{\rm BH})^4], \qquad (22)$$

where, for simplicity, we assumed that the magnetic field at the event horizon is comparable to that at the ergobelt, i.e., $B^2_{r=r_+} \approx B_0^2 = \sigma_0 w_0$, and where the magnetic flux across the horizon is given by $\Phi_{\rm H} \approx 4\pi B_0 r_+^2$. The bottom part of Figure 3 reports the ratio $\dot{E}_{\rm rec}/\dot{E}_{\rm BZ}$, showing that for sufficiently large BH spins and magnetizations the plasmoid-driven PP leads to an energy extraction that is smaller but comparable to that associated with the BZ mechanism. Figure 3 invites a comparison with Figure 7 in L. Comisso & F. A. Asenjo (2021), where $\dot{E}_{\rm rec}/\dot{E}_{\rm BZ}$ was also computed assuming plasmoids generated from an equatorial current sheet and having Keplerian velocities. When making such a comparison, we should take into account differences in the physical regimes considered and in the approximations made. In particular, since we consider an accretion scenario, we limit the magnetization to regimes that are compatible with the simulations and hence consider $\sigma_0 \lesssim 20$ (L. Comisso & F. A. Asenjo 2021 consider instead $\sigma_0 \lesssim 10^6$). Furthermore, the magnetic flux considered by L. Comisso & F. A. Asenjo (2021) includes a factor proportional to $\sin\xi$, where ξ is the "orientation angle," that is, the angle between the radial and azimuthal directions of the plasmoid velocity as measured in the comoving frame. The inclusion of this angular dependence, which is unsual for a surface-integrated flux that should not depend on the orientation angle, decreases the BZ power by a factor $\sin^2\xi$, thus magnifying the ratio by $\sim$15 for $\xi = \pi/12$ (which is the value considered in Figure 7 of L. Comisso & F. A. Asenjo 2021). When ignoring this factor and considering similar values of magnetization, our estimates of $\dot{E}_{\rm rec}/\dot{E}_{\rm BZ}$ are comparable to those computed by L. Comisso & F. A. Asenjo (2021) and by K. Parfrey et al. (2019) for electrons undergoing a PP.

4. Conclusions

Responding to the increasing evidence that resistive effects in plasmas around BHs play an important role in shaping the observed phenomenology of these objects, we have presented a general approach to the study of a PP driven by plasmoids produced at reconnection sites along current sheets. Our formalism ultimately establishes the physical conditions to make a plasmoid-driven PP energetically viable and can be applied equally to scenarios that are dominated by the plasma or by the magnetic field, that is, in MHD or FFE regimes. It is also genuinely multidimensional, and hence allows one to explore conditions that are beyond those studied so far and that have been restricted to the equatorial plane. In this sense, it provides a direct contact with numerical simulations, either in MHD (J. F. Mahlmann et al. 2020; A. Nathanail et al. 2020, 2021; B. Ripperda et al. 2020, 2022; I. Dimitropoulos et al. 2024) or with PIC approaches (K. Parfrey et al. 2019; I. El Mellah et al. 2022, 2023; J. Vos et al. 2024), all of which highlight an intense reconnection activity outside the equatorial plane. Finally, it does not assume an ad hoc description of the

dynamics of the plasma, or conjecture as to its kinematic properties with oversimplified and possibly unrealistic configurations. On the contrary, it constructs the dynamics of the plasma starting from a well-known configuration, that of an equilibrium torus with a toroidal magnetic field, and thus possessing all the features necessary to compute self-consistently the reconnection process and estimate the PP energetics.

While the results presented here offer the first coherent approach to a multidimensional treatment of the PP driven by magnetic reconnection, they can be improved in a number of ways. First, by developing a more accurate descriptions of plasmoids that could overcome the limitations of the RAIB model. Second, by exploiting the results of numerical simulations to produce better estimates of the reconnection rate and hence of the efficiency of the energy-extraction process. Third, by connecting the plasmoid production at the ergobelt with the plasmoid production on the equatorial plane (which remains a favorable site for the production of plasmoids), and hence join the MHD regime of the plasma in the torus with the FFE regime when the plasma has left the torus and is accreting onto the BH. We plan to investigate these important aspects in future works.

Acknowledgments

We thank Benoît Cerutti, Luca Comisso, Ileyk El Mellah, Claudio Meringolo, Antonios Nathanail, and Kyle Parfrey for insightful discussions and comments. Partial funding comes from the State of Hesse within the Research Cluster ELEMENTS (Project ID 500/10.006), by the ERC Advanced Grant "JETSET: Launching, propagation and emission of relativistic jets from binary mergers and across mass scales" (grant No. 884631). L.R. acknowledges the Walter Greiner Gesellschaft zur Förderung der physikalischen Grundlagenforschung e.V. through the Carl W. Fueck Laureatus Chair.

Data Availability

All data are incorporated into the Letter and its online supporting information.

Appendix

In what follows, we provide the most important details about the calculations or considerations needed to obtain the results presented in the main text.

Appendix A
Kerr Metric and ZAMO Frame

The Kerr metric in Boyer–Lindquist (BL) coordinates $x^\mu = (t, r, \theta, \phi)$ and in a (3+1) form reads $ds^2 = g_{\mu\nu}dx^\mu dx^\nu = -\mathrm{a}^2dt^2 + \gamma_{ij}(dx^i + \beta^i dt)(dx^j + \beta^j dt)$ with the lapse function, the shift vector, and the absolute space metric, respectively, defined as

$$\alpha = \frac{1}{\sqrt{-g^{tt}}} = \sqrt{\frac{\Delta\Sigma}{\Pi}}, \quad \beta^i = \alpha^2 g^{ti} = -\alpha^2 \frac{2Mar}{\Delta\Sigma}\delta^i_\phi,$$
$$\gamma_{ij}dx^i dx^j = \Sigma/\Delta\, dr^2 + \Sigma\, d\theta^2 + \Pi/\Sigma \sin^2\theta\, d\phi^2, \tag{A1}$$

and the metric determinant decomposes as $g = -\alpha^2 \det(\gamma_{ij})$. The metric functions explicitly read $\Delta = r^2 - 2Mr + a^2$, $\Sigma = r^2 + a^2\cos^2\theta$, and $\Pi = (r^2 + a^2)^2 - a^2\Delta\sin^2\theta$, with the event horizon position given by the r_+ root of $\Delta = (r - r_+)(r - r_-)$, $r_\pm = M(1 \pm \sqrt{1 - a_*^2})$, and the ergosphere location at $r_0(\theta) = M(1 + \sqrt{1 - a_*^2\cos^2\theta})$, where $a_* := a/M$. We assume the BH to have $0 \leqslant a_* \leqslant 1$, with the upper bound imposed by the cosmic censorship conjecture. Other interesting locations in the BH equatorial plane, $\theta = \pi/2$, are given by the marginally stable corotating (+) and counter-rotating (−) circular orbit, $r_{\mathrm{ms},\pm}$, and by the marginally bound circular orbit $r_{\mathrm{ms},\pm}$, depicted in Figure 4.

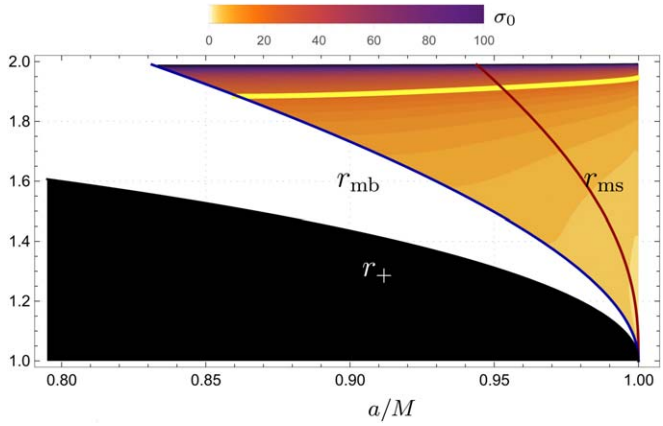

Figure 4. The same as Figure 2 but for $\theta = \pi/2$ and illustrating the (r, a) dependence. For each BH spin, the torus cusp is located between r_{mb} (black line) and r_{ms} (red line). Maximally filled tori penetrate the ergosphere ($r_0 = 2\,M$ on the equator) for $a/M \gtrsim 0.83$. Tori with the cusp at the largest possible position ($r_{\mathrm{cusp}} = r_{\mathrm{ms}}$ or $\ell_0 = \ell_{\mathrm{ms}}$) require larger BH spins, $a/M \gtrsim 0.94$. By increasing the BH spin $r_{\mathrm{ms}} \to r_{\mathrm{mb}} \to r_+$, the ergobelt area grows and comparatively smaller magnetizations are needed for a plasmoid-mediated PP.

The ZAMO is a normal observer (the corresponding 1-form in BL coordinates is $\boldsymbol{\eta} = -\alpha\boldsymbol{dt}$), with an associated local Cartesian right-handed frame $\hat{\boldsymbol{e}}_{(\alpha)} = (\hat{\boldsymbol{e}}_{(T)}, \hat{\boldsymbol{e}}_{(X)}, \hat{\boldsymbol{e}}_{(Y)}, \hat{\boldsymbol{e}}_{(Z)})$ specified by the vectors $\hat{\boldsymbol{e}}_{(T)} = \boldsymbol{\eta}$, $\hat{\boldsymbol{e}}_{(X)} = \boldsymbol{\partial_r}/\sqrt{\gamma_{rr}}$, $\hat{\boldsymbol{e}}_{(Y)} = \boldsymbol{\partial_\phi}/\sqrt{\gamma_{\phi\phi}}$, and $\hat{\boldsymbol{e}}_{(Z)} = -\boldsymbol{\partial_\theta}/\sqrt{\gamma_{\theta\theta}}$, and form a tetrad, namely, $g_{\mu\nu} = \hat{e}^{(\alpha)}_\mu \hat{e}^{(\beta)}_\nu \hat{\eta}_{(\alpha)(\beta)}$ and $\varepsilon_{\mu\nu\rho\sigma} = \hat{e}^{(T)}_\mu \wedge \hat{e}^{(X)}_\nu \wedge \hat{e}^{(Y)}_\rho \wedge \hat{e}^{(Z)}_\sigma$, where $\hat{\eta}_{(\alpha)(\beta)}$ is the Minkowski metric in the local frame and $\varepsilon_{\mu\nu\rho\sigma} := \sqrt{-g}\,\eta_{\mu\nu\rho\sigma}$ is the four-dimensional Levi-Civita tensor.

Appendix B
Plasma Velocity

As mentioned in the main text, the character of the field is set by the invariant quantity $F^{\mu\nu}F_{\mu\nu} = 2(\mathcal{B}^2 - \mathcal{E}^2)$, with the strength of the ZAMO fields given by

$$\mathcal{B}^2 = \frac{1}{\sin^2\theta}\left[\frac{\Delta(\partial_r\Psi)^2 + (\partial_\theta\Psi)^2}{\Pi} + \frac{I^2}{\Delta}\right],$$
$$\mathcal{E}^2 = \mathcal{F}^2(\Omega)\frac{\Delta(\partial_r\Psi)^2 + (\partial_\theta\Psi)^2}{\Pi\sin^2\theta}, \tag{B1}$$

and where we introduced $\mathcal{F}(\Omega) := \sqrt{\gamma_{\phi\phi}}(\omega_{\mathrm{Z}} - \Omega)/\alpha$. Notice that $\mathcal{F}(\Omega) = \pm 1$ at the outer/inner light surfaces, i.e., the locations where corotating observers with the field lines become null, $|\partial_t + \Omega(\Psi)\partial_\phi|^2 = \alpha^2(\mathcal{F}^2(\Omega) - 1) = 0$, or, equivalently, where the magnetic field transitions from being dominated by poloidal to toroidal components.

The orthonormal vectors (see Equation (6) in the main text), valid for degenerate fields, are conveniently parametrized in

terms of two magnetic orientation angles $\xi_1 := \tan^{-1}(\hat{\mathcal{B}}^{(Y)}/\hat{\mathcal{B}}^{(X)})$ and $\xi_2 := \cos^{-1}(\hat{\mathcal{B}}^{(Z)}/\sqrt{\mathcal{B}^2})$ with respect to the ZAMO frame, such that

$$\sin\xi_1 = -\sqrt{\Pi}\, I/\sqrt{\Delta(\partial_\theta\Psi)^2 + \Pi I^2}\,,$$
$$\sin\xi_2 = \sqrt{(\Pi I^2 + \Delta(\partial_\theta\Psi)^2)/(\Pi I^2 + \Delta(\Delta(\partial_r\Psi)^2 + (\partial_\theta\Psi)^2))}\,, \tag{B2}$$

with explicit expressions given by

$$\begin{aligned}
\boldsymbol{\mathcal{X}} &= \mathcal{X}^{(\alpha)}\hat{\boldsymbol{e}}_{(\alpha)} = (\cos\xi_2/\chi)\,\hat{\boldsymbol{e}}_{(X)} \\
&\quad - (\cos\xi_1\sin\xi_2/\chi)\,\hat{\boldsymbol{e}}_{(Z)} \\
\boldsymbol{\mathcal{Y}} &= \mathcal{Y}^{(\alpha)}\hat{\boldsymbol{e}}_{(\alpha)} = \cos\xi_1\sin\xi_2\,\hat{\boldsymbol{e}}_{(X)} \\
&\quad + \sin\xi_1\sin\xi_2\,\hat{\boldsymbol{e}}_{(Y)} + \cos\xi_2\,\hat{\boldsymbol{e}}_{(Z)}, \\
\boldsymbol{\mathcal{Z}} &= \mathcal{Z}^{(\alpha)}\hat{\boldsymbol{e}}_{(\alpha)} = -(\cos\xi_1\sin\xi_1\sin^2\xi_2/\chi)\,\hat{\boldsymbol{e}}_{(X)} + \chi\,\hat{\boldsymbol{e}}_{(Y)} \\
&\quad - (\cos\xi_2\sin\xi_1\sin\xi_2/\chi)\,\hat{\boldsymbol{e}}_{(Z)},
\end{aligned} \tag{B3}$$

where $\chi := \sqrt{1 - (\sin\xi_1\sin\xi_2)^2}$.

As anticipated in the main text, it is possible to use such a set of vectors to construct the most general four-velocity that is compatible with the electric field screening condition. More specifically, the velocity perpendicular to the fields can be written as $\hat{v}_\perp^2 = \mathcal{F}^2(\Omega)(1 - \hat{\mathcal{B}}^2_{(Y)}/\mathcal{B}^2)$. The parallel component, instead, can be parametrized as $\hat{v}_\parallel := q\hat{v}_\parallel^{\max} = q/\hat{\gamma}$, with $q \in (-1, 1)$ and $\hat{\gamma} = \hat{\gamma}_\perp/\sqrt{1 - q^2}$. In the ZAMO Cartesian frame, the components of the spatial velocity read

$$\hat{v}^{(X)} = \left(\mathcal{F}\frac{\hat{\mathcal{B}}^{(Y)}}{\mathcal{B}} + q\sqrt{1 - \mathcal{F}^2\left(1 - \frac{\hat{\mathcal{B}}^2_{(Y)}}{\mathcal{B}^2}\right)}\right)\frac{\hat{\mathcal{B}}^{(X)}}{\mathcal{B}}, \tag{B4}$$

$$\hat{v}^{(Y)} = \mathcal{F}\left(\frac{\hat{\mathcal{B}}^2_{(Y)}}{\mathcal{B}^2} - 1\right) + q\sqrt{1 - \mathcal{F}^2\left(1 - \frac{\hat{\mathcal{B}}^2_{(Y)}}{\mathcal{B}^2}\right)}\frac{\hat{\mathcal{B}}^{(Y)}}{\mathcal{B}}, \tag{B5}$$

$$\hat{v}^{(Z)} = \left(\mathcal{F}\frac{\hat{\mathcal{B}}^{(Y)}}{\mathcal{B}} + q\sqrt{1 - \mathcal{F}^2\left(1 - \frac{\hat{\mathcal{B}}^2_{(Y)}}{\mathcal{B}^2}\right)}\right)\frac{\hat{\mathcal{B}}^{(Z)}}{\mathcal{B}}, \tag{B6}$$

where $0 \leqslant q \leqslant 1$ is a free coefficient and where the expressions above reduce to the previous results in the literature under the appropriate limits.[9] Furthermore, it is easy to verify that the components in Equations (B4) and (B6) satisfy the standard relation $\hat{v}^{(X)}/\hat{\mathcal{B}}^{(X)} = \hat{v}^{(Z)}/\hat{\mathcal{B}}^{(Z)}$.

Appendix C
On the Magnetized Torus

Equations (B4)–(B6) show that if the magnetic field is purely toroidal, $\hat{\boldsymbol{\mathcal{B}}} = \hat{\mathcal{B}}^{(Y)}\hat{\boldsymbol{e}}_{(Y)}$, the same is true for the plasma velocity $\hat{\boldsymbol{v}} = q\,\hat{\boldsymbol{e}}_{(Y)}$, so that the velocity is purely parallel to the field lines. This is the basic dynamical property of the plasma in a Komissarov torus. Furthermore, the condition for the four-velocity to be that of a circular motion with angular velocity Ω_0 as seen by an asymptotic observer requires that $\hat{v}_\parallel = q = \mathcal{F}(\Omega_0)$. We here are interested in tori with a constant specific angular momentum $\ell_0 := u_\phi/u_t$ and corotating with the BH ($\ell_0 = \text{const.} > 0$), so that the magnetic field is aligned with the azimuthal coordinate, i.e., $\Psi = 0$ and $I < 0$, so that $\xi_{1,2} = \pi/2$ (see Equation (B2)). In this case, $\Omega_0 := -(g_{t\phi} + g_{tt}\ell_0)/(g_{\phi\phi} + g_{t\phi}\ell_0)$, and we can express the parallel velocity as a function of ℓ_0 as $\hat{v}_\parallel = \alpha\ell_0/[\sqrt{\gamma_{\phi\phi}}(\omega_Z\ell_0 - 1)]$. With these assumptions, together with the condition $\tilde{v}_{\rm out} \approx \sqrt{\sigma_0/(1+\sigma_0)}$ and $\tilde{\gamma}_{\rm out} \approx \sqrt{1+\sigma_0}$ (Y.-H. Liu et al. 2017), Equation (14) reduces to

$$\varepsilon^\infty_\pm = \alpha\hat{\gamma}\left[\left(1 + \frac{\sqrt{\gamma_{\phi\phi}}}{\alpha}\omega_Z\quad \hat{v}_\parallel\right)\sqrt{1+\sigma_0} \pm \left(\hat{v}_\parallel + \frac{\sqrt{\gamma_{\phi\phi}}}{\alpha}\omega_Z\right)\sqrt{\sigma_0} - \frac{1}{4}\frac{\sqrt{1+\sigma_0} - \hat{v}_\parallel\sqrt{\sigma_0}}{\hat{\gamma}^2(1+\sigma_0-\hat{v}_\parallel^2\sigma_0)}\right]. \tag{C1}$$

We should note that although we derive Equation (C1) as a limit of Equation (14) for $\hat{v}_\parallel = \alpha\ell_0/[\sqrt{\gamma_{\phi\phi}}(\omega_Z\ell_0 - 1)]$ and $\tilde{v}_{\rm out} \approx \sqrt{\sigma_0/(1+\sigma_0)}$, it coincides with Equation (34) in L. Comisso & F. A. Asenjo (2021), where the plasma was assumed to be in a Keplerian circular orbit in the equatorial plane. Within these limits, therefore, Equation (34) in L. Comisso & F. A. Asenjo (2021) would provide a multidimensional expression for the plasmoid energies when the Keplerian velocity is replaced by a generic nonplanar one.

We notice that the comoving magnetic field satisfies $b^t = \ell_0 b^\phi$, as is typical in a Komissarov torus (S. S. Komissarov 2004), with $b^t = -\hat{v}_\parallel\hat{\gamma}_\parallel\hat{\mathcal{B}}^{(Y)}/\alpha$.[10] The torus is traditionally defined by equipotential surfaces specified by the condition (M. Abramowicz et al. 1978; M. Kozlowski et al. 1978)

$$\mathcal{W} = \frac{1}{2}\ln\left|\frac{\alpha^2\gamma_{\phi\phi}}{\gamma_{\phi\phi}(1 - \ell_0\omega_Z)^2 - \alpha^2\ell_0^2}\right| = \text{const.} \tag{C2}$$

We label with $\mathcal{W}_{\rm cusp}$ the equipotential surface intersecting the equatorial plane at the corresponding cusp radius $r_{\rm cusp}$, for which the angular momentum matches the Keplerian value $\ell_0 = \ell_\kappa$, and whose value is solely specified in terms of ℓ_0 and a, whereas $\mathcal{W}_{\rm in}$ labels the torus's inner edge, which must be specified as a boundary condition. Furthermore, the choice of ℓ_0 uniquely determines the locations of the cusp and of the position of the (pressure) rest-mass density maximum, and is constrained to be $\ell_0 > \ell_{\rm ms}$ (L. Rezzolla & O. Zanotti 2013). If $\ell_{\rm ms} \leqslant \ell_0 \leqslant \ell_{\rm mb}$, then $\mathcal{W}_{\rm cusp}$ is guaranteed to be nonpositive, so that matter and fields can fill the torus up to the cusp, $\mathcal{W}_{\rm in} \leqslant \mathcal{W}_{\rm cusp}$. In the limiting case $\ell_0 = \ell_{\rm mb}$, the outermost equipotential surface is marginally closed, i.e., $\mathcal{W}_{\rm cusp} = 0$, while if $\mathcal{W}_{\rm in} = 0$ the torus is said to be maximally filled. Conversely, if $\ell_0 > \ell_{\rm mb}$, then $\mathcal{W}_{\rm cusp} > 0$, and matter never reaches the cusp being confined within the regions where $\mathcal{W}_{\rm in} < 0$. In our construction, we always consider tori that are maximally filled, $\mathcal{W}_{\rm in} = \mathcal{W}_{\rm cusp} = 0$, since this arguably represents the most interesting configuration, with the torus configuration fully specified by the BH spin and with matter at the cusp prone to accrete onto the BH if perturbed.

[9] For $q = 0$, Equations (B4)–(B6) coincide with (D140) in A. Chael et al. (2023), and for $q = 1$ with (A12) in S. S. Komissarov (2004). Furthermore, the following relations hold: $\hat{\mathcal{B}}^{(X)} = \sqrt{\gamma_{rr}}\hat{\mathcal{B}}^r$, $\hat{\mathcal{B}}^{(Y)} = \sqrt{\gamma_{\phi\phi}}\hat{\mathcal{B}}^\phi$, and $\hat{\mathcal{B}}^{(Z)} = -\sqrt{\gamma_{\theta\theta}}\hat{\mathcal{B}}^\theta$.

[10] In the notation used in S. S. Komissarov (2004), $b^\phi = \pm\sqrt{2p_m/\mathcal{A}}$, where $p_m := b^2/2 = \hat{\mathcal{B}}^2_{(y)}/2$ and $\mathcal{A} := g_{\phi\phi} + 2\ell_0 g_{t\phi} + \ell_0^2 g_{tt} = \alpha^2\ell_0^2(1 - \hat{v}_\parallel^2)/\hat{v}_\parallel^2$.

The area of the ergobelt is determined by an implicit equation $\mathcal{W}_{\rm in}(r,\,\theta) = \mathcal{W}_0$. Because of the nontrivial location of the ergobelt, the surface differential $d\mathcal{A}$ is given by $d\mathcal{A} = \sqrt{\gamma_{\phi\phi} d\phi^2}\sqrt{\gamma_{\theta\theta} d\theta^2 + \gamma_{rr} dr^2}\,|_{\mathcal{W}_0}$, with $\phi \in [0,\,2\pi]$ and $\theta \in [\theta_\star,\,\pi/2]$, where $\theta_\star$ is the polar angle that limits the effective region from above at given σ_0, ℓ_0 and a. The minimum value $\theta_\star^{\rm m}$ (i.e., the maximum of the integral support, corresponding to the optimal condition $\sigma_0 \gg 1$) can be determined analytically by inverting Equation (C2) with the supplementary condition $r = r_0(\theta_\star^{\rm m})$, so that

$$\cos(2\theta_\star^{\rm m}) = 1 + \frac{4f_0\ell_0}{a_* M(1-2f_0)} + \frac{4f_0}{a_*^2(1-2f_0)^2} \times (f_0 - 1 + \sqrt{(f_0-1)^2 - a_*^2(1-2f_0)^2 + 2a_*\ell_0 f_0(2f_0-1)/M}), \tag{C3}$$

where $f_0 := e^{2\mathcal{W}_0}$. For a maximally filled torus, $f_0 = 1$, and $\cos(2\theta_\star^{\rm m}) = 1 - 4\ell_0/a + 4M\sqrt{2\ell_0 - a}\,/a^{3/2}$, which consistently leads to $\theta_\star^{\rm m} = \pi/2$ for $a_{\rm crit} = 2(\sqrt{2}-1)M$.

Appendix D
Relativistic Adiabatic Incompressible Balls

In what follows, we recall the calculation of the energy-at-infinity of a RAIB starting from the energy-momentum tensor of an ideal fluid, following the original discussion of S. Koide & K. Arai (2008). The hydrodynamic energy and angular momentum as measured by a ZAMO can be obtained by projecting the fluid part of the energy-momentum tensor $T^{\mu\nu}_{\rm fl}$ (i.e., not containing electromagnetic contributions) over the ZAMO tetrad:

$$\hat{e}_{\rm fl} := T^{(T)(T)}_{\rm fl} = -p + w\hat{\gamma}^2, \quad \hat{\ell}_{\rm fl} := T^{(T)(Y)}_{\rm fl} = w\hat{\gamma}^2\hat{v}^{(Y)}, \tag{D1}$$

where $T^{\mu\nu}_{\rm fl} := wu^\mu u^\nu + pg^{\mu\nu}$, with w and p the enthalpy density and the pressure measured in the comoving frame of the fluid, respectively, and $\hat{\gamma}$ the Lorentz factor of the fluid with respect to the ZAMO. The conserved Noether currents in stationary and axisymmetric hydrodynamic flows, $\mathcal{J}^\mu_E = -T^\mu_\nu(\partial_t)^\nu$ and $\mathcal{J}^\mu_L = T^\mu_\nu(\partial_\phi)^\nu$, can be expressed as combinations of quantities measured in the ZAMO frame, with their redshifted temporal components being respectively the energy density and angular-momentum-at-infinity, $e^\infty = \alpha\hat{e} + \sqrt{\gamma_{\phi\phi}}\omega_Z\hat{\ell}$ and $\ell^\infty = \sqrt{\gamma_{\phi\phi}}\;\;\hat{\ell}$.

Assuming the fluid to be perfect and described by an ideal-fluid equation of state, the pressure can be expressed as $p = \rho\epsilon(\Gamma - 1)$, with Γ the adiabatic index, ρ the rest-mass density, and ϵ the specific internal energy. As a result, the enthalpy density is $w = \rho(1 + \epsilon\Gamma) = \rho + 4p$ for a completely degenerate relativistic fluid with $\Gamma = 4/3$ (L. Rezzolla & O. Zanotti 2013). For simplicity, we assume that the rest-mass density of the plasmoid is much smaller than the internal energy density, i.e., $\rho \ll \rho\epsilon$, so that the enthalpy density can be approximated as $w = \rho + 4p \approx 4p$. Future improvements to the approach followed here (and in the literature) will concentrate on better estimating not only the role of the rest-mass density over the internal energy density, but also on the role played by the magnetization in the plasma.

Bearing these considerations in mind, we recall that the RAIB model assumes that the rest-mass density is localized, so that, in the ZAMO frame, $\rho = m\delta^3(\hat{\boldsymbol{x}} - \hat{\boldsymbol{x}}(t))/\hat{\gamma}(t)$, where m is the rest mass of the RAIB. This allows one to easily integrate the energy and angular momentum density over the entire three-space in the ZAMO frame to obtain the total energy and angular-momentum-at-infinity associated with a RAIB:

$$E^\infty_{\rm RAIB} = \alpha\left[H\hat{\gamma}\left(1 + \frac{\sqrt{\gamma_{\phi\phi}}}{\alpha}\omega_Z\hat{v}^{(Y)}\right) - \frac{U(\Gamma-1)}{\hat{\gamma}}\right],$$
$$L^\infty_{\rm RAIB} = \sqrt{\gamma_{\phi\phi}}\quad H\hat{\gamma}\hat{v}^{(Y)}\,. \tag{D2}$$

In obtaining the expressions above, we have written the total enthalpy as $H = m(1 + \epsilon\Gamma)$ and the total internal energy as $U = m\epsilon$ (Equation (D2) coincides with Equation (14) in the main text).

We conclude this appendix by clarifying an inconsistency often encountered in the literature that adopts the RAIB prescription. It should be noted that in L. Comisso & F. A. Asenjo (2021, see Equation (25) therein), and in many related works the expression above is improperly identified as an energy density. The inconsistency becomes evident once it is realized that if Equation (25) in L. Comisso & F. A. Asenjo (2021) corresponds to an energy density, it can be further integrated in space to obtain the total energy, and upon taking the pointlike particle limit (i.e., $U = 0$ and $H = m$) in flat spacetime ($\alpha = 1$ and $\omega_Z = 0$), this would lead to $E = m$. Conversely, the pointlike particle limit in flat spacetime of Equation (14) leads to the correct result for the total relativistic energy of a single particle, i.e., $E = m\hat{\gamma}$.

ORCID iDs

Filippo Camilloni https://orcid.org/0000-0003-0412-0491
Luciano Rezzolla https://orcid.org/0000-0002-1330-7103

References

Abramowicz, M., Jaroszynski, M., & Sikora, M. 1978, A&A, 63, 221
Aimar, N., Dmytriiev, A., Vincent, F. H., et al. 2023, A&A, 672, A62
Akiyama, K., Alberdi, A., Alef, W., et al. 2019, ApJL, 875, L5
Anderson, M., Hirschmann, E. W., Lehner, L., et al. 2008, PhRvL, 100, 191101
Asenjo, F. A., & Comisso, L. 2015, PhRvL, 114, 115003
Asenjo, F. A., & Comisso, L. 2017, PhRvL, 118, 055101
Bañados, M., Silk, J., & West, S. M. 2009, PhRvL, 103, 111102
Ball, D., Özel, F., Psaltis, D., Chan, C.-K., & Sironi, L. 2018, ApJ, 853, 184
Bardeen, J. M., Press, W. H., & Teukolsky, S. A. 1972, ApJ, 178, 347
Bejger, M., Piran, T., Abramowicz, M., & HÅkanson, F. 2012, PhRvL, 109, 121101
Beloborodov, A. M. 2017, ApJ, 850, 141
Berti, E., Brito, R., & Cardoso, V. 2015, PhRvL, 114, 251103

Blandford, R. D., & Znajek, R. L. 1977, MNRAS, 179, 433
Bosch, P., Green, S. R., & Lehner, L. 2016, PhRvL, 116, 141102
Bransgrove, A., Ripperda, B., & Philippov, A. 2021, PhRvL, 127, 055101
Camilloni, F., Dias, O. J. C., Grignani, G., et al. 2022, JCAP, 2022, 032
Cassak, P. A., Liu, Y. H., & Shay, M. A. 2017, JPlPh, 83, 715830501
Chael, A., Lupsasca, A., Wong, G. N., & Quataert, E. 2023, ApJ, 958, 65
Chen, B., Hou, Y., Li, J., & Shen, Y. 2024, PhRvD, 110, 063003
Comisso, L., & Asenjo, F. A. 2014, PhRvL, 113, 045001
Comisso, L., & Asenjo, F. A. 2021, PhRvD, 103, 023014
Crinquand, B., Cerutti, B., Dubus, G., Parfrey, K., & Philippov, A. 2022, PhRvL, 129, 205101
Dadhich, N., Tursunov, A., Ahmedov, B., & Stuchlìk, Z. 2018, MNRAS, 478, L89
Dimitropoulos, I., Nathanail, A., Petropoulou, M., & Contopoulos, I. 2024, A&A, submitted, arXiv:2407.14312
Dionysopoulou, K., Alic, D., & Rezzolla, L. 2015, PhRvD, 92, 084064
East, W. E., & Pretorius, F. 2017, PhRvL, 119, 041101
El Mellah, I., Cerutti, B., & Crinquand, B. 2023, A&A, 677, A67
El Mellah, I., Cerutti, B., Crinquand, B., & Parfrey, K. 2022, A&A, 663, A169
Event Horizon Telescope Collaboration, Akiyama, K., Alberdi, A., et al. 2022, ApJL, 930, L16
Fan, Z.-Y., Li, Y., Zhou, F., & Guo, M. 2024, PhRvD, 110, 104044
Gelles, Z., Chael, A., & Quataert, E. 2025, ApJ, 981, 204
Gimeno-Soler, S., & Font, J. A. 2017, A&A, 607, A68
Gralla, S. E., & Jacobson, T. 2014, MNRAS, 445, 2500
Guo, F., Li, H., Daughton, W., & Liu, Y.-H. 2014, PhRvL, 113, 155005
Huang, Y.-M., & Bhattacharjee, A. 2012, PhRvL, 109, 265002
Kiuchi, K., Sekiguchi, Y., Kyutoku, K., et al. 2015, PhRvD, 92, 064034
Koide, S., & Arai, K. 2008, ApJ, 682, 1124
Komissarov, S. S. 2004, MNRAS, 350, 427
Komissarov, S. S. 2006, MNRAS, 368, 993
Kozlowski, M., Jaroszynski, M., & Abramowicz, M. A. 1978, A&A, 63, 209
Landau, L. D., & Lifshitz, E. M. 2004, The Classical Theory of Fields, Course of Theoretical Physics, Vol 2 (Oxford: Elsevier Butterworth-Heinemann)
Lasota, J. P., Gourgoulhon, E., Abramowicz, M., Tchekhovskoy, A., & Narayan, R. 2014, PhRvD, 89, 024041
Liu, Y.-H., Guo, F., Daughton, W., Li, H., & Hesse, M. 2015, PhRvL, 114, 095002
Liu, Y.-H., Hesse, M., Guo, F., et al. 2017, PhRvL, 118, 085101
Liu, Y. T., Shapiro, S. L., Etienne, Z. B., & Taniguchi, K. 2008, PhRvD, 78, 024012
Lyubarsky, Y. E. 2005, MNRAS, 358, 113
Mahlmann, J. F., Levinson, A., & Aloy, M. A. 2020, MNRAS, 494, 4203
McKinney, J. C. 2006, MNRAS, 367, 1797
Meringolo, C., Cruz-Osorio, A., Rezzolla, L., & Servidio, S. 2023, ApJ, 944, 122
Mizuno, Y., & Rezzolla, L. 2024, arXiv:2404.13824
Montero, P. J., Zanotti, O., Font, J. A., & Rezzolla, L. 2007, MNRAS, 378, 1101
Nathanail, A., & Contopoulos, I. 2014, ApJ, 788, 186
Nathanail, A., Fromm, C. M., Porth, O., et al. 2020, MNRAS, 495, 1549
Nathanail, A., Gill, R., Porth, O., Fromm, C. M., & Rezzolla, L. 2021, MNRAS, 502, 1843
Palenzuela, C., Lehner, L., Ponce, M., et al. 2013, PhRvL, 111, 061105
Palenzuela, C., Lehner, L., Reula, O., & Rezzolla, L. 2009, MNRAS, 394, 1727
Pani, P., Cardoso, V., Gualtieri, L., Berti, E., & Ishibashi, A. 2012, PhRvL, 109, 131102
Parfrey, K., Philippov, A., & Cerutti, B. 2019, PhRvL, 122, 035101
Penrose, R., & Floyd, R. M. 1971, Natur, 229, 177
Press, W. H., & Teukolsky, S. A. 1972, Natur, 238, 211
Rezzolla, L., Giacomazzo, B., Baiotti, L., et al. 2011, ApJL, 732, L6
Rezzolla, L., & Zanotti, O. 2013, Relativistic Hydrodynamics (Oxford: Oxford Univ. Press)
Ripperda, B., Bacchini, F., & Philippov, A. A. 2020, ApJ, 900, 100
Ripperda, B., Bacchini, F., Porth, O., et al. 2019, ApJS, 244, 10
Ripperda, B., Liska, M., Chatterjee, K., et al. 2022, ApJL, 924, L32
Ruffini, R., Prakapenia, M., Quevedo, H., & Zhang, S. 2025, PhRvL, 134, 081403
Schnittman, J. D. 2014, PhRvL, 113, 261102
Shen, Y., & YuChih, H.-Y. 2025, PhRvD, 111, 023003
Su, Y., Veronig, A. M., Holman, G. D., et al. 2013, NatPh, 9, 489
Tchekhovskoy, A., Narayan, R., & McKinney, J. C. 2010, ApJ, 711, 50
Thorne, K. S., & Macdonald, D. 1982, MNRAS, 198, 339
Uzdensky, D. A. 2005, ApJ, 620, 889
Uzdensky, D. A., & Spitkovsky, A. 2013, ApJ, 780, 3
Vos, J., Cerutti, B., Moscibrodzka, M., & Parfrey, K. 2024, arXiv:2410.19061
Yamada, M., Kulsrud, R., & Ji, H. 2010, RvMP, 82, 603
Zweibel, E. G., & Yamada, M. 2009, ARA&A, 47, 291